

Original research

F. nucleatum targets lncRNA ENO1-IT1 to promote glycolysis and oncogenesis in colorectal cancer

Jie Hong ,¹ Fangfang Guo,¹ Shi-Yuan Lu ,¹ Chaoqin Shen,¹ Dan Ma,¹ Xinyu Zhang,¹ Yile Xie,¹ Tingting Yan,¹ TaChung Yu,¹ Tiantian Sun,¹ Yun Qian,¹ Ming Zhong,² Jinxian Chen,² Yanshen Peng,¹ Cheng Wang,³ Xiang Zhou,³ Jianjun Liu,³ Qiang Liu,⁴ Xiong Ma ,¹ Ying-Xuan Chen,¹ Haoyan Chen ,¹ Jing-Yuan Fang ¹

► Additional material is published online only. To view please visit the journal online (<http://dx.doi.org/10.1136/gutjnl-2020-322780>).

For numbered affiliations see end of article.

Correspondence to

Dr Jing-Yuan Fang, State Key Laboratory for Oncogenes and Related Genes; Key Laboratory of Gastroenterology & Hepatology, Ministry of Health; Division of Gastroenterology and Hepatology, Shanghai Institute of Digestive Disease, Renji Hospital, School of Medicine, Shanghai Jiao Tong University., Shanghai, China; jingyuanfang@sjtu.edu.cn
Dr Jie Hong; jiehong97@sjtu.edu.cn
Dr. Haoyan Chen; haoyanchen@sjtu.edu.cn

JH, FG and S-YL contributed equally.

Received 11 August 2020
Revised 22 November 2020
Accepted 29 November 2020

ABSTRACT

Objective Microbiota disorder promotes chronic inflammation and carcinogenesis. High glycolysis is associated with poor prognosis in patients with colorectal cancer (CRC). However, the potential correlation between the gut microbiota and glucose metabolism is unknown in CRC.

Design ¹⁸F-FDG (¹⁸F-fluorodeoxyglucose) PET (positron emission tomography)/CT image scanning data and microbiota PCR analysis were performed to measure the correlation between metabolic alterations and microbiota disorder in 33 patients with CRC. Multiple colorectal cancer models, metabolic analysis and Seahorse assay were established to assess the role of long non-coding RNA (lncRNA) enolase1-intronic transcript 1 (ENO1-IT1) in *Fusobacterium (F.) nucleatum*-induced glucose metabolism and colorectal carcinogenesis. RNA immunoprecipitation and chromatin immunoprecipitation sequencing were conducted to identify potential targets of lncRNA ENO1-IT1.

Results We have found *F. nucleatum* abundance correlated with high glucose metabolism in patients with CRC. Furthermore, *F. nucleatum* supported carcinogenesis via increasing CRC cell glucose metabolism. Mechanistically, *F. nucleatum* activated lncRNA ENO1-IT1 transcription via upregulating the binding efficiency of transcription factor SP1 to the promoter region of lncRNA ENO1-IT1. Elevated ENO1-IT behaved as a guider modular for KAT7 histone acetyltransferase, specifying the histone modification pattern on its target genes, including ENO1, and consequently altering CRC biological function.

Conclusion *F. nucleatum* and glucose metabolism are mechanistically, biologically and clinically connected to CRC. Targeting ENO1 pathway may be meaningful in treating patients with CRC with elevated *F. nucleatum*.

Significance of this study

What is already known on this subject?

- Colorectal cancer (CRC) is one of the most common cancers.
- The majority of the patients are recurrent for drug resistance, and are generally not responding to immune checkpoint therapy.
- Metabolic disruption, abnormal glycolysis in particular, promotes cancer progression and prognosis.
- *Fusobacterium (F.) nucleatum* is reported to be an oncobacterium in cancers, including CRC.
- Long non-coding-RNAs (lncRNAs) contribute to carcinogenesis.

What are the new findings?

- *F. nucleatum* promotes glucose metabolism in CRC cells and clinically correlates with high ¹⁸F-FDG (¹⁸F-fluorodeoxyglucose) uptake in patients with CRC.
- *F. nucleatum* upregulates lncRNA enolase1-intronic transcript 1 (ENO1-IT1) transcription via transcription factor SP1.
- LncRNA ENO1-IT guides KAT7 histone acetyltransferase to specify the histone modification pattern on its target genes, including ENO1.
- The effect of *F. nucleatum* on cancer metabolism reprogramming is different from the previously reported mechanisms.

How might it impact on clinical practice in the foreseeable future?

- Our findings have made a connection between tumour metabolism and environmental cue, and provided a novel angle in dissecting colorectal carcinogenesis.
- Targeting the ENO1 pathway presents a promising approach to treat patients with CRC with high amount of *F. nucleatum*.

Check for updates

© Author(s) (or their employer(s)) 2020. No commercial re-use. See rights and permissions. Published by BMJ.

To cite: Hong J, Guo F, Lu S-Y, et al. Gut Epub ahead of print: [please include Day Month Year]. doi:10.1136/gutjnl-2020-322780

INTRODUCTION

Colorectal cancer (CRC) is the third most common cancer and the second leading cause of cancer-related death worldwide.^{1 2} The majority of the patients with CRC eventually experience tumour recurrence due to drug resistance.³ Notably, patients with CRC are generally not responsive to current immune checkpoint therapy.^{4 5} To explore effective treatment options, there is an urgent need to

dissect the novel mechanisms underlying colorectal carcinogenesis.

Cancer cell growth depends on energy supplement. Disruption of energy metabolism, especially abnormal glycolysis, is a hallmark of cancer.⁶ Potent

glucose metabolism has been observed in patients with various types of cancer.⁷ Imaging ¹⁸F-fluorodeoxyglucose (¹⁸F-FDG) radioactive tracer allows to track solid tumours and evaluate tumour characteristics in patients with positron emission tomography-CT (PET/CT).⁸ CRC may produce a large amount of lactic acid and accelerate the acidification of the tumour micro-environment via enhanced glycolysis.⁹ Recently, we and others have reported that *Fusobacterium* (*F.*) *nucleatum* promotes carcinogenesis and chemoresistance of CRC.^{10,11} However, the correlation of and the mechanism behind intestinal microbiota disorders with abnormal activation of glycolysis in CRC progression remains to be determined.

Here, we explored whether and how the cross-talk between microbiota and glucose metabolism affected colorectal carcinogenesis. We used real-time PCR analysis to detect the abundance and diversity of the intestinal flora in tissue samples from patients with CRC, and corroborated these results with the ¹⁸F-FDG PET/CT scanning data. We found the amount of *F. nucleatum* is increased in patients with CRC with higher glucose metabolism, compared with those with lower glucose metabolism. We reported that *F. nucleatum* affected CRC glycolysis via targeting the axis of long non-coding RNA (lncRNA) enolase1-intronic transcript 1 (ENO1-IT1) and KAT7 histone modification.

RESULTS

F. nucleatum correlates with high glucose metabolism in CRC

To explore metabolic alterations in CRC, we collected imaging information on 33 patients with CRC, who were diagnosed as primary CRC and received ¹⁸F-FDG PET/CT scanning before radical surgery (Cohort 1). We observed CRC tissues exhibit varying capabilities in absorbing ¹⁸F-FDG (online supplemental figure 1A), which indicated the heterogeneity of glucose metabolism in individual patients and has been chosen as a hallmark of tumour glycolytic metabolism.¹² To identify potential connection between gut microbiota and glycolytic metabolism in CRC, we performed real-time PCR analysis for several well-known commensal and oncogenic bacterial species of CRC¹³ in Cohort 1 (figure 1A; online supplemental figure 1B). We observed the most significant correlations between ¹⁸F-FDG uptake and the abundance of *F. nucleatum* in patients with CRC of Cohort 1 (figure 1A,B), as integrated analysis between ¹⁸F-FDG maximum uptake values (SUV_{max}) and real-time PCR assays. This finding was validated in an independent CRC patient data set (Cohort 2) (figure 1C; online supplemental figure 1C); online supplemental table S1), while no significant correlation were detected between SUV_{max} and other clinical factors like total bacterial abundance, tumour size and KRAS mutation and so on in patients with CRC in Cohort 2 (online supplemental file S1D-S1L); online supplemental table S1). The positive correlation between the high amount of *F. nucleatum* and activated glycolysis-related pathways were additionally validated in The Cancer Genome Atlas (TCGA) database (figure 1D). The data indicates that *F. nucleatum* closely correlates with the glycolysis pathway activation in CRC.

To functionally test this hypothesis, we first co-cultured different CRC cells with *F. nucleatum* and measured lactic acid production. Colorimetric assay showed that upregulated lactic acid production were the most significant in HCT116 and DLD1 cells in response to *F. nucleatum* treatment, compared with other CRC cells (online supplemental figure S1M). We next performed liquid chromatography-coupled tandem mass spectrometry (LC-MS)-based assay followed by detecting metabolites in HCT116 cells (figure 1E). *F. nucleatum* treatment

significantly increased the level of key metabolic components of the glycolysis pathway, such as D-Fructose-1,6-bisphosphate and 3-Phospho-D-glycerate in HCT116 cells (figure 1E, left panel). Real-time PCR and western blot assay confirmed that *F. nucleatum* affected the levels of key components of glycolysis pathway, such as hexokinase2 (HK2), enolase 1 (ENO1) and lactic dehydrogenase A (LDHA) in CRC cells (figure 1E, right panel; online supplemental figure S1N-P).

Next, we questioned whether *F. nucleatum* levels directly influenced CRC glycolytic metabolism. We cultured HCT116 (figure 1F-H; online supplemental figure S1S) and DLD1 cells (figure 1I; online supplemental figure S1R-T) with *F. nucleatum* or non-pathogenic *E.coli* (DH5α), and then measured lactate production, glucose uptake level, extracellular acidification rate (ECAR) and oxygen consumption rate (OCR). We found that *F. nucleatum* incubation significantly increased lactate production (figure 1F; online supplemental figure S1Q) and glucose uptake level (figure 1G; online supplemental figure S1R). We also found enhanced ECAR levels (figure 1H1) in HCT116 and DLD1 cells, but not OCR levels (online supplemental figure S1R, T).

F. nucleatum is associated with colorectal carcinogenesis.¹⁴⁻¹⁶ We examined whether *F. nucleatum*-induced cell proliferation depends on glycolysis pathway in CRC. Cell proliferation assay showed that *F. nucleatum* significantly increased cell proliferation and DNA replication in HCT116 (figure 1J; online supplemental figure S1U) and DLD1 (online supplemental figure S1V, W) cells, while 2-DG (an inhibitor of glycolysis pathway) treatment significantly blocked *F. nucleatum*-induced cell proliferation in vitro. We inoculated HCT116 cells into nude mice and treated the mice with *F. nucleatum* and 2-DG. As expected, *F. nucleatum* inoculation-induced tumour growth was efficiently abrogated by 2-DG (figure 1K; online supplemental figure S1Y, X). The ¹⁸F-FDG Micro-PET data of tumour glucose uptake showed that *F. nucleatum*-induced tumour glycolysis was significantly blocked by 2-DG in tumour xenografts in nude mice (figure 1L; online supplemental figure S1Z), indicating that *F. nucleatum* may alter tumour glycolytic metabolism and affect colorectal carcinogenesis.

F. nucleatum activates glycolysis and carcinogenesis via a selective increase of lncRNA ENO1-IT1

Environmental elements often affect CRC progression via epigenetic alteration; including microRNA, lncRNA and histone modification.¹⁷⁻¹⁹ We hypothesised that *F. nucleatum* may target non-coding RNAs to promote glycolysis and tumorigenesis in CRC. To test this hypothesis, we performed two independent global transcriptome profiling experiments in both *F. nucleatum* treated CRC cell lines and human CRC tissues bearing various abundance of *F. nucleatum* (figure 2A; cohort 3). Hundreds of lncRNAs were found to be altered in CRC cells after *F. nucleatum* treatment and in CRC tissues with high amount of *F. nucleatum*, compared with control. We next chose three lncRNAs with highest correlation coefficient with tumour *F. nucleatum* abundance for further validation. Among them, real-time PCR analysis in CRC cells and patients indicated that lncRNA ENSG00000236269.1 was significantly increased after *F. nucleatum* treatment in HCT116 cells, and this lncRNA was higher in patients with cancer with high amount of *F. nucleatum* (online supplemental figure S2A-C). Furthermore, only knockdown of lncRNA ENSG00000236269.1 (ENO1-IT1) significantly blocked lactic acid production in HCT116 cells at the basal condition (online supplemental figure S2D, E). Therefore, we focussed our studies on ENO1-IT1. Next

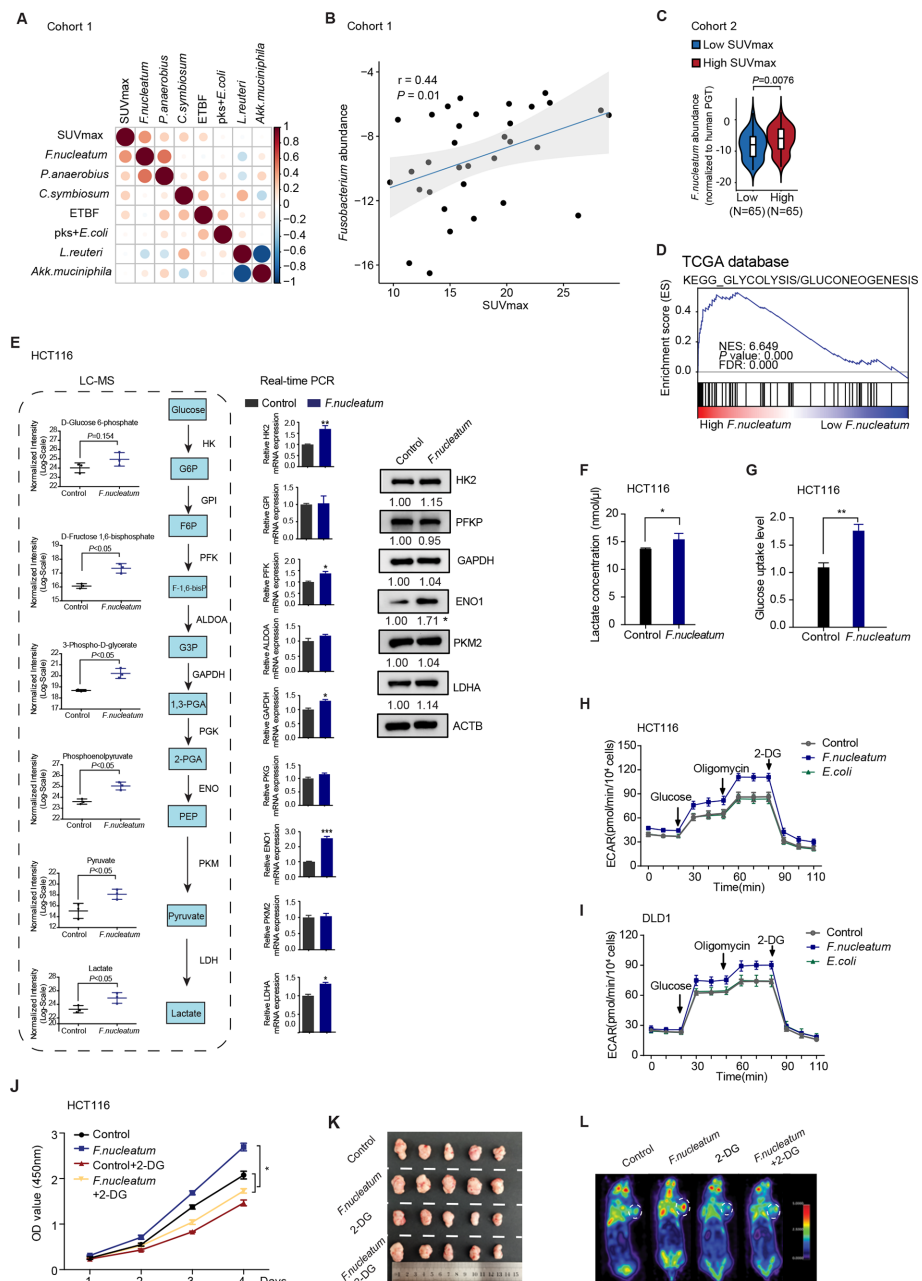


Figure 1 *F. nucleatum* correlates with high glucose metabolism in CRC. (A) Spearman's correlation between taxa enrichment and ¹⁸F-FDG uptake in patients with CRC by real-time PCR (data pooled from Cohort 1, n=33). (B) Spearman's correlation between *F. nucleatum* abundance and SUVmax in Cohort 1. (C) Statistical analysis between the quantity of *F. nucleatum* and SUVmax (data pooled from Cohort 2, n=106, the high and low SUVmax was defined via median). (D) GSEA analysis about glycolysis/gluconeogenesis-related gene profiles based on *F. nucleatum* abundance in TCGA database. (E) Alteration of intermediate metabolites of glycolysis by targeted LC-MS/MS (n=3, left panel) and glycolysis-related gene expression analysis by qRT-PCR (n=3) and western blot (n=3) in HCT116 cells with or without *F. nucleatum* co-culture (right panel); densitometry of western blotting bands was quantified by ImageJ software of two independent experiments (gray-scale band analysis) and normalised to control. (F–G) Lactate concentration level (F) and glucose uptake amount (G) of HCT116 cells on 2 hours co-culture with *F. nucleatum* (data pooled from three independent assay, n=3). (H–I) ECAR levels of HCT116 (H, n=6) and DLD1 (I, n=6) cells with or without *F. nucleatum* or non-pathogenic *E. coli* co-culture. (J) Cell proliferation assay of HCT116 cells on 2 hours co-cultured with *F. nucleatum* in the presence of 2-DG (n=6). (K) Representative images of tumours in mice under different conditions; mice were treated with *F. nucleatum* or/with 2-DG (n=5 out of 8). (L) Representative PET/CT images in mice under different conditions. All data are means±SEM. *p<0.05, **p<0.01, ***p<0.001, n.s., not significant. One-way ANOVA in (J); two-tailed Student's t-test in (E–G); non-parametric Mann-Whitney U test in (C and L); Spearman correlation test in (A and B). ANOVA, analysis of variance; CRC, colorectal cancer; ECAR, extracellular acidification rate; GSEA, gene set enrichment analysis; LC-MS, liquid chromatography-coupled tandem mass spectrometry; PET, positron emission tomography; SUVmax, maximum uptake values; TCGA, The Cancer Genome Atlas; ¹⁸F-FDG, ¹⁸F-fluorodeoxyglucose.

Colon

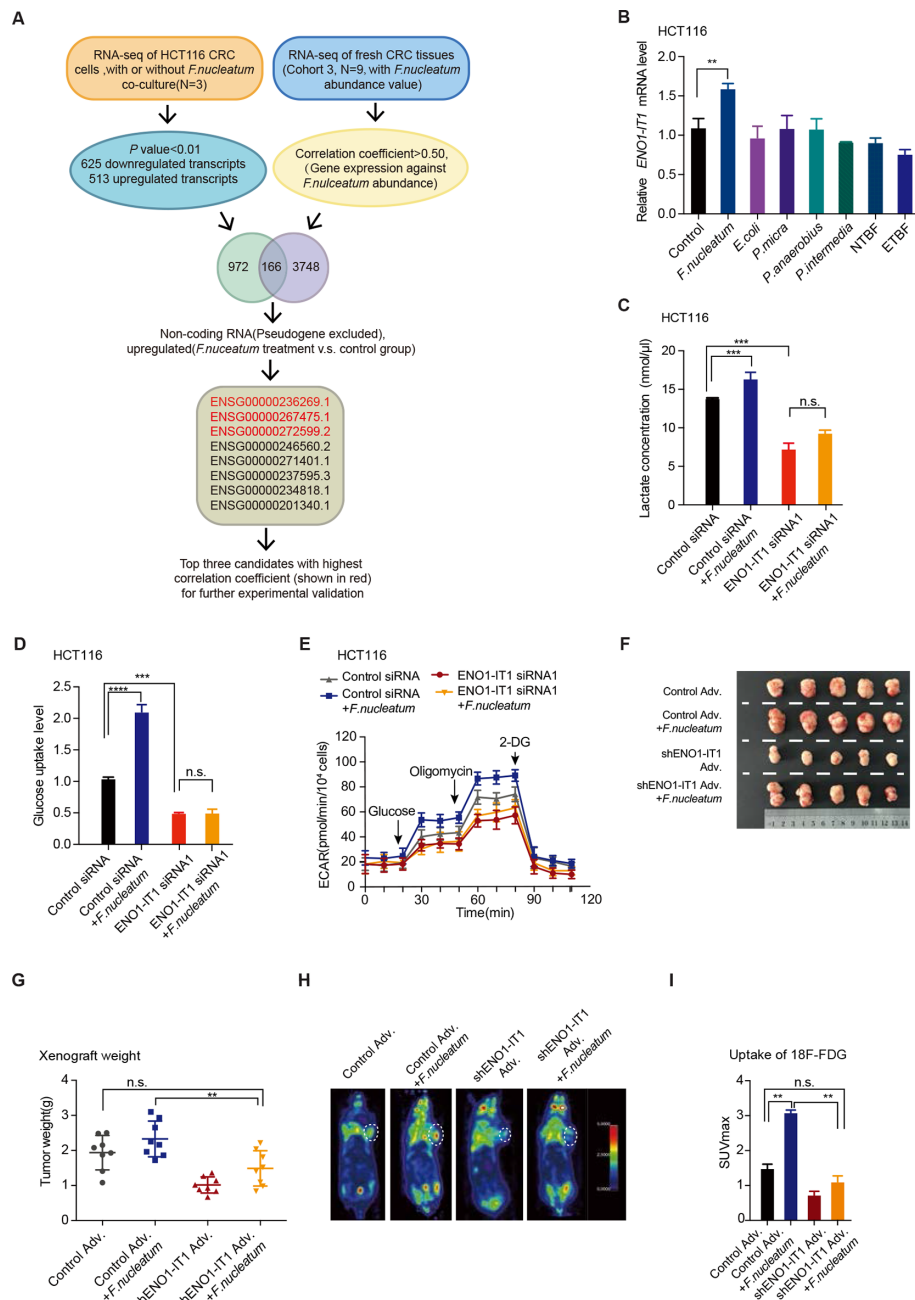


Figure 2 *F. nucleatum* activates glycolysis and carcinogenesis via a selective increase of lncRNA ENO1-IT1. (A) Flow chart for selecting candidate lncRNAs, regulated by *F. nucleatum*. (B) Real-time PCR to show ENO1-IT1 expression induction in HCT116 cells with different bacteria co-culture (normalised to control cells, data pooled from three independent assay, n=3). (C–D) lactate concentration (C) and glucose uptake amount (D) in HCT116 cells co-cultured with *F. nucleatum* with/or ENO1-IT1 siRNA1 transfection (data pooled from three independent assay, n=3). (E) ECAR levels in different groups of HCT116 cells co-cultured with *F. nucleatum* with/or ENO1-IT1 siRNA1 transfection (n=6/group). (F) Representative images of tumours in mice under different conditions. (G) Statistical analysis of tumour weights(n=8/group).(H–J) Representative PET/CT images (H) and average ¹⁸F-FDG SUVmax of two out of eight xenograft tumours (J) in mice under different conditions; mice were treated with adenovirus or/with *F. nucleatum*. Adenovirus symbolled as Adv. All data are means±SEM **p<0.01, ***p<0.001, ****p<0.0001, n.s., not significant. One-way ANOVA in (B–E); non-parametric Mann-Whitney U test in (G and I). ANOVA, analysis of variance; ECAR, extracellular acidification rate; ENO1-IT1, enolase 1-intronic transcript 1; lncRNA, long non-coding RNA; PET, positron emission tomography; siRNA, small interfering RNA; SUVmax, maximum uptake values; ¹⁸F-FDG, ¹⁸F-fluorodeoxyglucose.

validation assay revealed ENO1-IT1 may be specifically upregulated by *F. nucleatum* in CRC cells (figure 2B and online supplemental figure 2F, G). LncRNA ENO1-IT1 was predicted to be a lncRNA rather than a protein-coding transcript by northern blot (online supplemental figure S2H) and in vitro translation analysis (online supplemental figure S2I). (RACE)-PCR assay and

sequencing data identified the 5' ends and the transcription start site of ENO1-IT1 (online supplemental figure 2J, K). Furthermore, ENO1-IT1 was mainly located in the nucleus of CRC cells by real-time PCR assay (online supplemental figure S2L). Collectively, we concluded that ENO1-IT1 is a novel lncRNA.

To demonstrate whether ENO1-IT1 mediated the biological function of *F. nucleatum* in CRC, we knocked down ENO1-IT1 by ENO1-IT1 small interfering RNA (siRNA) in HCT116 cells and treated these cells with *F. nucleatum*. We found that the *F. nucleatum*-induced increase in lactate production (figure 2C), glucose uptake (figure 2D) and ECAR level (figure 2E; online supplemental figure S2M) were abolished by knocking down ENO1-IT1 in HCT116 cells, indicating that ENO1-IT1 mediated the biological function of *F. nucleatum* in CRC cells. Furthermore, we observed that *F. nucleatum*-induced increase in tumour growth (figure 2F; online supplemental figure S2N), tumour weight (figure 2G) and tumour volume (online supplemental figure S2O) were significantly blocked by inhibition of ENO1-IT1 in xenograft mouse models. Furthermore, micro-PET scans showed that *F. nucleatum*-manifested increase in glucose uptake *in vivo* was prevented by sh-ENO1-IT1 (figure 2H).

In gain of function assay, overexpression of ENO1-IT1 acted synergistically with *F. nucleatum* to stimulate an increase in nuclear lncRNA expression (online supplemental figure S2P, Q), lactate production (online supplemental figure S2R), glucose uptake (online supplemental figure S2S) and cell proliferation (online supplemental figure S2T) in DLD1 cells. These data suggest that ENO1-IT1 plays an essential role in *F. nucleatum* mediated-glycolysis activation and cell proliferation in CRC.

ENO1-IT1 coordinates the acetylation of histone genome-wide via KAT7

LncRNAs participate in a wide-spectrum of biological processes; including epigenetic modifications, *et al.*²⁰ To explore the underlying mechanism of ENO1-IT1-mediated glycolysis and carcinogenesis in CRC, we sought to identify intracellular ENO1-IT1-binding factors in an unbiased manner (figure 3A). Biotinylated ENO1-IT1 and negative control were incubated with total protein extracts from HCT116 cells and pulled down with streptavidin. There was one specific band in the ENO1-IT1 pull-down samples after SDS-PAGE analysis and Coomassie Brilliant Blue staining (figure 3B). We excised and analysed the band by mass spectrometry (MS). MS analysis revealed 300 potential binding proteins in the band. Among these binding proteins, we selected the top 10 proteins that likely participated in transcription regulation for binding validation. Western blot analysis showed that seven proteins; including KAT7 (HBO1/Myst2) (figure 3C), bound specifically to ENO1-IT1, but not CTCF, STAT1 or CDC73 (online supplemental figure SA3). Then, we detected reduced lactate levels in HCT116 cells transfection of siKAT7, but not other siRNAs of those seven genes (online supplemental figure S3B-D). These data suggest that the KAT7 may interact with ENO1-IT1 to modulate glycolysis in CRC cells.

KAT7 belongs to the MYST protein family, which is the catalytic subunits of histone acetyltransferase (HAT) complexes and can regulate cell proliferation and DNA repair in the development of organisms and cancer.^{21 22} To identify the KAT7-interacting region of ENO1-IT1, we constructed and biotinylated two fragments of lncRNA, and used them in the RNA pull-down assay with HCT116 cell lysates. We found that the 3' fragment of ENO1-IT1 mediated the interaction with KAT7 (figure 3D). To substantiate the observation, anti-KAT7 antibody was used to immunoprecipitate endogenous KAT7 and the binding RNAs from nuclear extracts of HCT116 cells. PCR data (figure 3E,F) and fluorescent *in situ* hybridisation (online supplemental figure S3E) revealed that ENO1-IT1 directly co-localised with KAT7 in HCT116 cells.

KAT7 is a histone acetyltransferase. We explored the histone modification site modified by KAT7 in CRC cells. Western blot data showed that only H3K27Ac level was significantly decreased, but not other site after knockdown of KAT7 in HCT116 cells (figure 3G; online supplemental figure S3F). To address whether ENO1-IT1 modulated KAT7 genomic binding genome-wide, we performed chromatin immunoprecipitation coupled with high-throughput sequencing (ChIP-seq) for KAT7 and the potential modification site of the acetyltransferase H3K27Ac in HCT116 cells. KAT7 ChIP-seq data revealed that knockdown of ENO1-IT1 caused significantly decreased KAT7 occupancies in the histone modulator binding DNA regions compared with control HCT116 cells (figure 3H).

Further analysis showed that knockdown of ENO1-IT1 led to a concordant decrease of KAT7 occupancies in 62% of KAT7 occupied gene promoter regions. The promoter regions of these genes correspondingly decreased the levels of H3K27Ac (figure 3H), the potential histone acetylation products of KAT7. Furthermore, the promoter regions of 49 potential target genes were regulated both by KAT7 and H3K27Ac modification. According to the bioinformatics analysis and literature investigation, 10 out of the 49 genes may regulate cancer metabolism and progression (figure 3I). Further real-time PCR data showed that 3 of the 10 potential target genes (ENO1, MALAT1 and NDUFC1) were significantly increased by *F. nucleatum* inoculation in HCT116 cells (online supplemental figure S3G), which displayed lower KAT7 and H3K27Ac modification levels after knockdown of ENO1-IT1 (figure 3J; online supplemental figure S3H, I). Knockdown of ENO1-IT1 dramatically blocked *F. nucleatum*-induced ENO1 upregulation, but not MALAT1 or NDUFC1, in HCT116 cells (figure 3K). Therefore, we chose ENO1 for additional investigation.

ENO1-IT1 interacts with KAT7 to regulate ENO1 in CRC

According to the ChIP-seq data analysis, ENO1 is one of the target genes of KAT7/ENO1-IT1 complex. ENO1 is a key glycolytic enzyme that catalyses the conversion of 2-phosphoglycerate to phosphoenolpyruvate (PEP).²³ Interestingly, ENO1-IT1 is located at the first intron of ENO1 gene. Based on the cis-regulatory effects of some lncRNAs on nearby genes, we hypothesised that ENO1-IT1 may modulate CRC glycolysis by epigenetic regulation of ENO1 gene. Expression data showed that ENO1 expression was significantly decreased in HCT116 cells transfected with two different ENO1-IT1 siRNAs (online supplemental figure S4A, B). In contrast, overexpression of ENO1-IT1 significantly increased ENO1 expression in DLD1 cells (online supplemental figure S4C, D). To explore the mechanism by which ENO1-IT1 induced upregulation of ENO1, we performed bioinformatics analysis in genome database. According to the UCSC genome database analysis, both (NM_001201483.4) ENO1 and ENO1-IT1 are located in the chr1: 8861000–8878686 region (online supplemental figure S4E). We selected the DNA fragment containing 1000 bp upstream of the first exon of ENO1 and 100 bp after the transcription start site (represented by black slash boxes) to construct the luciferase reporter plasmid of ENO1 (pGL3-pENO1). Through DNA sequence alignment analysis, we found that there is a 678 bp gap between the upstream of ENO1-IT1 exon1 and the end of the ENO1 exon1. Therefore, we selected this 678 bp DNA fragment (represented by green slash boxes) for constructing the luciferase reporter plasmid of ENO1-IT1 (pGL3-pENO1-IT1). Luciferase assay showed that both of the ENO1 and ENO1-IT1 candidate promoter fragments successfully initiated the reporter gene transcription

Colon

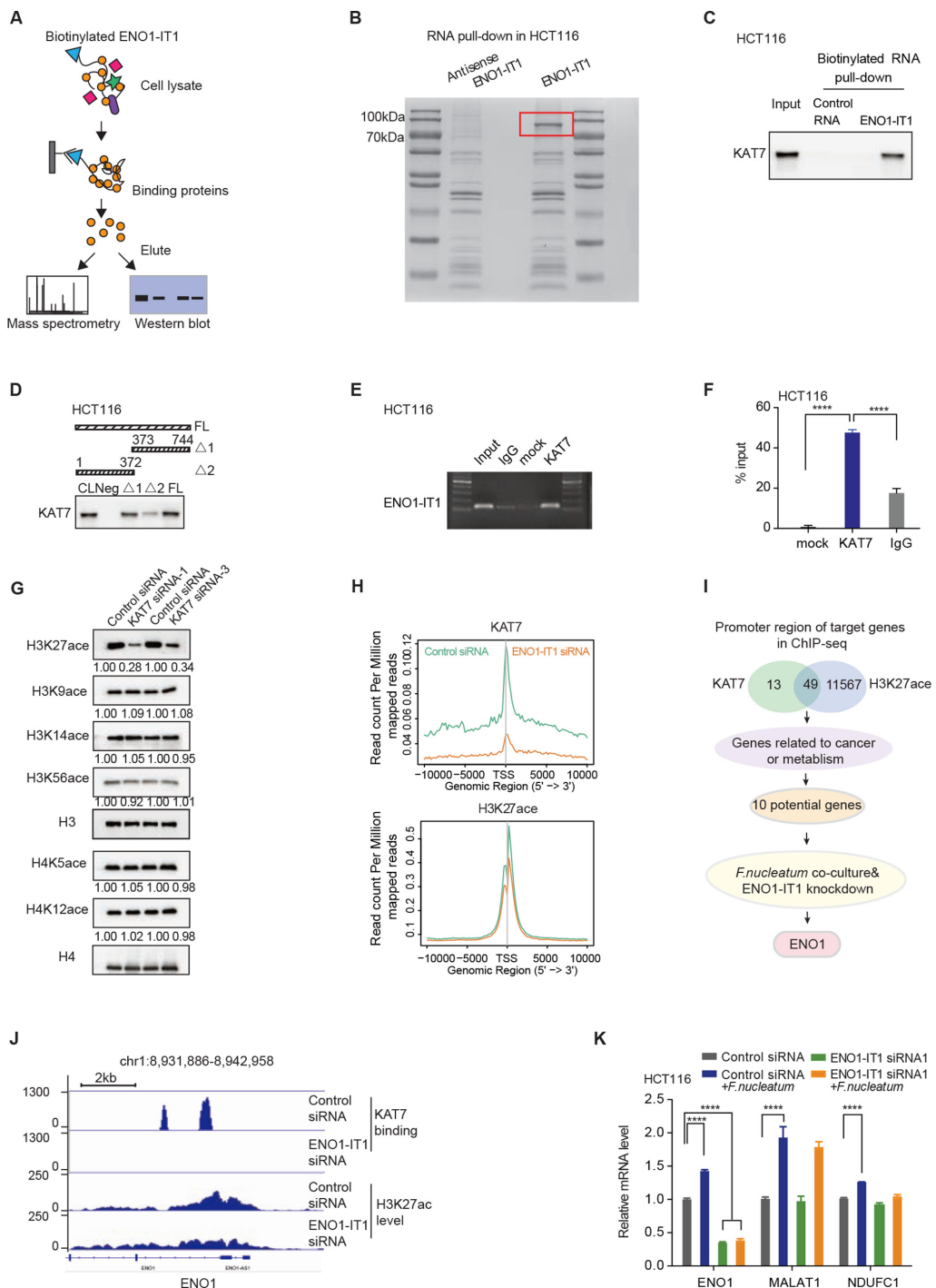


Figure 3 ENO1-IT1 coordinates the acetylation of histone genome-wide via KAT7. (A) Experimental design for RNA pull-down assays and downstream verifications of potential targeting proteins. (B) Coomassie Brilliant Blue staining of biotinylated ENO1-IT1-associated proteins. One ENO1-IT1-specific band (in frame) was excised and analysed by mass spectrometry. (C) Western blot of proteins from control RNA and ENO1-IT1 RNA pull-down assays, n=3. (D) Western blot of KAT7 in samples pulled down by full-length (FL) of sense lncRNA ENO1-IT1 or truncated ENO1-IT1 ($\Delta 1$: 373 to 744, $\Delta 2$: 1 to 372), with SDS serving as negative control (Neg) and cell lysis (CL) as positive control, n=2. (E–F) RNA immunoprecipitation experiments were performed using anti-KAT7 antibody, and specific primers were used to detect ENO1-IT1 (E, n=2). The complexes were analysed for the presence of ENO1-IT1 by real-time PCR (F, n=2), results represent means of two independent experiments. *p<0.05, **p<0.01 (Student's t-test). (G) HCT116 cells were transfected with KAT7 siRNAs and histone acetylation modification level at different sites were analysed after by western blot. Densitometry of western blotting bands was quantified by ImageJ software of two independent experiments (gray-scale band analysis, statistics in Extended Data figure 3e) and normalised to control siRNA. (H) Representation of genomic binding of gene promoters over a 20 kb window centred on each KAT7 (upper panel) and H3K27Ac (lower panel) ChIP-seq peaks in HCT116 cells after knockdown of ENO1-IT1. (I–J) Flow chart of sorted targeted genes of KAT7 and H3K27Ac modification (I) and example of ChIP-seq binding sites for KAT7 and the binding modification sites for H3K27Ac on ENO1 gene promoter was shown (J). (K) Real-time PCR to test mRNA expression analysis of selected genes in HCT116 cells co-cultured with *F. nucleatum* with/or ENO1-IT1 siRNA1 transfection(n=3). All data are means \pm SEM, ***p<0.0001. ChIP, chromatin immunoprecipitation; ENO1-IT1, enolase 1-intronic transcript 1; mRNA, messenger RNA; siRNA, small interfering RNA.

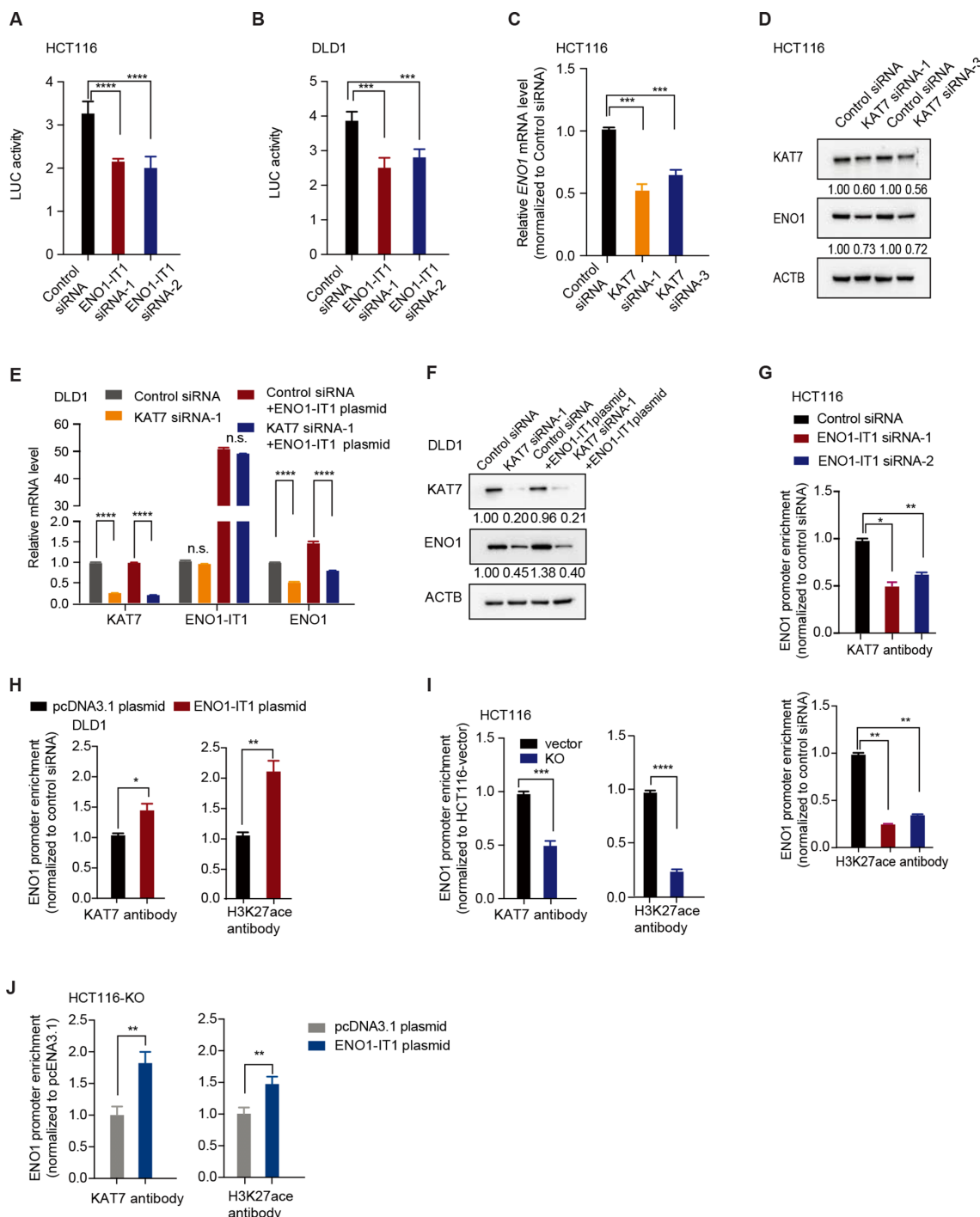


Figure 4 ENO1-IT1 interacts with KAT7 to regulate ENO1 in CRC. (A–B) Luciferase activity on ENO1 promoter region in HCT116 (A, n=6) and DLD1 (B, n=6) cells transfected with control or ENO1-IT1 siRNAs. (B–C) Real-time PCR (C) and western blot (D) detection of ENO1 expression in HCT116 cells after KAT7 siRNA transfection, n=3. (E–F) Real-time PCR (E) and western blot (F) detection of ENO1 expression in DLD1 cells after KAT7 siRNA transfection alone or with ENO1-IT1 plasmid, n=3. (G–J) Real-time PCR of the ChIP samples in detection of the binding efficiency of KAT7 or H3K27Ac to the ENO1 gene promoter after siRNAs or plasmid transfection in HCT116 (G, n=2), DLD1 (H, n=2), and CRISPR ENO1-IT1-KO (I and J, n=2) cells. All data are means \pm SEM *p<0.05, **p<0.01, ***p<0.001, ****p<0.0001, n.s., not significant. One-way ANOVA in (E); two-tailed Student's t-test in (A–C, G–J). Densitometry of western blotting bands was quantified by ImageJ software (gray-scale band analysis, statistics in online supplemental figure S4H, JJ) of two or three independent experiments, non-parametric Mann-Whitney U test. ANOVA, analysis of variance; CRC, colorectal cancer; ChIP, chromatin immunoprecipitation; ENO1-IT1, enolase 1-intronic transcript 1; siRNA, small interfering RNA.

(online supplemental figure S4F), respectively, indicating that there may be different promoters to drive ENO1-IT1 and ENO1 transcription. Further luciferase assays revealed that knockdown of ENO1-IT1 impaired the transcriptional level of the ENO1 promoter in HCT116 (figure 4A) and DLD1 (figure 4B) cells.

The data suggest that ENO1-IT1 may positively regulate ENO1 transcription in CRC, and the transcription of ENO1-IT1 and ENO1 may be driven by different promoters.

To investigate whether KAT7 is involved in the transcriptional regulation effects of ENO1-IT1 on ENO1 gene, we transfected

KAT7 siRNAs in HCT116 and DLD1 cells. Real-time PCR (figure 4C; online supplemental figure S4G) and western blot (figure 4D; online supplemental figure S4H, I) showed that knockdown of KAT7 significantly decreased ENO1 expression in CRC cells. Furthermore, knockdown of KAT7 significantly blocked ENO1-IT1-induced ENO1 upregulation in ENO1-IT1-expressing DLD1 cells (figure 4E,F; online supplemental figure S4J-L), suggesting that ENO1-IT1-induced upregulation of ENO1 gene relies on KAT7 histone acetyltransferase.

To understand whether KAT7 directly bound to the promoter region of ENO1, we performed ChIP assay in HCT116 and DLD1 cells (online supplemental figure S4M). Knockdown of ENO1-IT1 significantly decreased the binding efficiency of KAT7 to the ENO1 promoter region, as well as the H3K27Ac level in HCT116 cells (figure 4G). Hence, ENO1-IT1 may mediate KAT7 binding to the ENO1 gene promoter region. In gain of function assay, the similar effect was observed in DLD1 cells (figure 4H). We next used CRISPR/Cas9 system to knock out ENO1-IT1 in HCT116 cells (online supplemental figure S4N), and obtained similar results. Knockout of ENO1-IT1 significantly decreased the binding efficiency of KAT7 and reduced histone H3K27Ac levels at the ENO1 promoter region (figure 4I). Overexpression of ENO1-IT1 in the lncRNA knockout cells could compensate for these changes (figure 4J). Altogether, ENO1-IT1 may recruit KAT7 to the promoter of the ENO1 gene and regulate ENO1 transcription via epigenetic modulation.

F. nucleatum promotes CRC glycolysis via ENO1

To identify whether ENO1 gene was the downstream effector gene of *F. nucleatum*-mediated colorectal carcinogenesis and glycolysis, we performed real-time PCR and western blot to detect ENO1 expression in HCT116 and DLD1 cells after *F. nucleatum* incubation. *F. nucleatum* stimulation significantly upregulated ENO1 expression, and these effects were abolished by knockdown of ENO1-IT1 (figure 5A,B; online supplemental figure S5A). Meanwhile, overexpression of ENO1-IT1 promoted *F. nucleatum*-induced the upregulation of ENO1 expression in DLD1 cells (online supplemental figure 5B,C). Real-time ChIP PCR data showed that downregulation of ENO1-IT1 abolished *F. nucleatum*-induced binding efficiency of KAT7 and the H3K27Ac levels at the ENO1 promoter region (figure 5C), indicating the role of ENO1-IT1 in *F. nucleatum*-activated ENO1 transcription in CRC cells.

Moreover, *F. nucleatum*-induced lactate production (figure 5D), ECAR activation (figure 5E; online supplemental figure S5D), and cell proliferation (figure 5F) were abolished by knockdown of ENO1 in HCT116 cells (online supplemental figure S5E,F). Supporting this finding *in vivo*, *F. nucleatum*-induced tumour progression was abolished by knocking down ENO1 in CRC xenograft mouse models (figure 5G), as indicated by tumour weight (figure 5H) and tumour volume (online supplemental figure S5G). Furthermore, micro-PET scans showed *F. nucleatum*-induced increase in glucose uptake was blocked by knockdown of ENO1 (figure 5I; online supplemental figure S5H). Thus, down-regulation of ENO1 and ENO1-IT1 comparably impairs CRC cell glycolysis induced by *F. nucleatum*.

To explore which regulatory mechanism may be involved in the gene regulation induced by the *F. nucleatum*, we predicted 71 transcription factors that potentially regulate ENO1-IT1 expression from the CHIP BASE database analysis (<http://rna.sysu.edu.cn/chipbase/>). Correlation analysis was performed between expression of ENO1-IT1 and 71 transcription factors in TCGA data set (online supplemental table 5). Three transcription factors

(ELK4, BCLAF1, SP1) with correlation coefficient great than 0.35 were selected in further study (online supplemental figure S5I). Among them, SP1, was reported to be closely associated with glycolysis^{24 25} and activated by *Fusobacteria* infection.^{26 27} Knockdown of SP1, but not the other two genes significantly downregulated ENO1-IT1 (online supplemental figure S5J, K). Furthermore, luciferase assay (online supplemental figure S5L, M) and Chip assay (figure 5J; online supplemental figure S5N) data verified that SP1 directly bound to ENO1-IT1 promoter region, but not that of ENO1 (online supplemental figure S5O). Downregulation of SP1 dramatically decreased *F. nucleatum*-induced upregulation of ENO1-IT1 (figure 5K), lactate production (online supplemental figure S5P) and glucose uptake (online supplemental figure S5Q), suggesting that SP1 may mediate *F. nucleatum*-induced upregulation of ENO1-IT1, high lactate production and glucose uptake.

Levels of *F. nucleatum*, ENO1-IT1, and ENO1 correlate and predict CRC patient outcome

F. nucleatum induced glycolysis by upregulating the key components of glycolysis pathway in CRC. As glycolysis activation is common in chemotherapy failures,^{28–30} we hypothesised that patients with CRC harbouring a high amount of *F. nucleatum* were more sensitive to ENO1-targeted therapy. To test this, we treated HCT116 cells with the specific inhibitor of ENO1, ENOblock, after *F. nucleatum* inoculation. The colormetric assay showed that ENOblock treatment dramatically decreased *F. nucleatum*-induced increase in ENO1ase activity (figure 6A) and cell proliferation (figure 6B). We next examined the potential role of 2.5 μM ENOblock, which had no effect on HCT116 cell proliferation (online supplemental figure S6A), in the chemotherapy sensitivity of CRC cells. Tumour cell killing experimental data showed that ENOblock significantly increased oxaliplatin- and 5-FU-induced tumour inhibition rate in HCT116 cells with *F. nucleatum* inoculation (figure 6C,D), compared with control group.

In the CRC xenograft mouse models, HCT116 cells were inoculated into nude mice and followed by treatment with ENOblock. Administering ENOblock enhanced the effect of chemotherapeutic agents on *F. nucleatum*-conditioned tumour cell growth *in vivo* (figure 6E,F; online supplemental figure S6B-E). There was no difference in tumour weight (online supplemental figure S6B,D) and tumour volume (online supplemental figure S6C,E) among different control groups. Interestingly, tumour growth was significantly decreased by oxaliplatin (figure 6E) and 5-FU treatment (figure 6F), and these tumour decreases were blocked when tumour cells were cultured with *F. nucleatum*. ENOblock treatment dramatically increased tumour inhibition efficiency in tumour bearing mice treated with oxaliplatin (figure 6E; online supplemental figure S6B,C), 5-FU (figure 6F; online supplemental figure S6D,E) and also blocked tumour growth in mice inoculated with tumour cells cultured with *F. nucleatum* (figure 6E,F; online supplemental figure S6B-E). Thus, targeting ENO1 glycolytic enzyme may enhance the sensitivity of chemotherapy by inhibiting glycolysis in patients with CRC with high amount of *F. nucleatum*.

To investigate the clinical significance of *F. nucleatum*, ENO1-IT1 and ENO1 in patients with CRC, we quantified *F. nucleatum* and detected ENO1-IT1 and ENO1 levels in CRC tissues. Both ENO1-IT1 and ENO1 levels were increased in CRC tissues compared with para-cancer tissues (figure 6G-J; online supplemental figure S6F). Furthermore, the amount of *F. nucleatum* positively correlated with the levels of ENO1-IT1

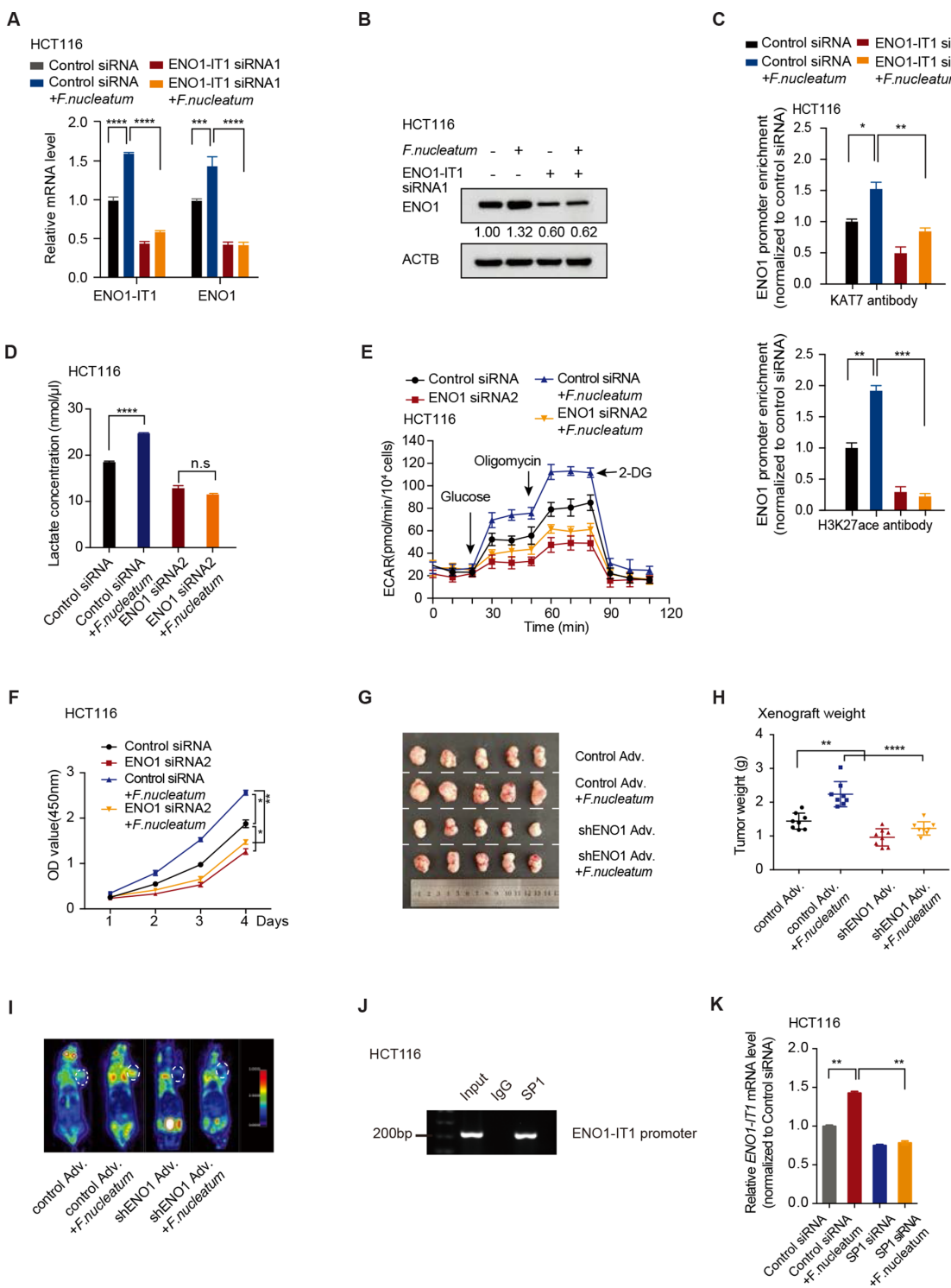


Figure 5 *F. nucleatum* promotes CRC glycolysis via ENO1. (A–B) Real-time PCR (A) and western blot (B) to detect ENO1 expression in HCT116 cells (n=3). (C) Binding efficiency of KAT7 or H3K27Ac to the ENO1 gene promoter in ChIP samples from HCT116 cells (n=2). In (A–C), Cells were analysed after ENO1-IT1 siRNA transfection with/ or *F. nucleatum* stimulation, results are mean±SEM of two or three independent experiments. (D) Lactate concentration level was determined in HCT116 cells(n=3). (E) ECAR levels in different groups of HCT116 cells(n=6). (F) Cell proliferation ability was detected in HCT116 cells. In (D–F), Cells were analysed after ENO1 siRNA transfection with/ or *F. nucleatum* stimulation, results are mean±SEM of two or three independent experiments (G) Representative images of tumours in mice under different conditions. (H) Statistical analysis of tumour weights in different groups, n=8/group, non-parametric Mann-Whitney U test. (I) Representative PET/CT images (Adenovirus symbolised as Adv.). (J) DNA was detected in the chromatin sample immunoprecipitated from HCT116 cells using an antibody against SP1, with IgG serving as negative control and input as positive control. (K) ENO1-IT1 mRNA analysis in HCT116 cells after SP1 siRNA transfection with/ or *F. nucleatum* stimulation, results are mean±SEM, n=3. *p<0.05, **p<0.01, ***p<0.001. One-way ANOVA test in (A, C, D, F, K); non-parametric Mann-Whitney U test in (E). ANOVA, analysis of variance; CRC, colorectal cancer; ChIP, chromatin immunoprecipitation; ECAR, extracellular acidification rate; ENO1-IT1, enolase 1-intron 1 transcript 1; mRNA, messenger RNA; PET, positron emission tomography; siRNA, small interfering RNA.

Colon

Figure 6

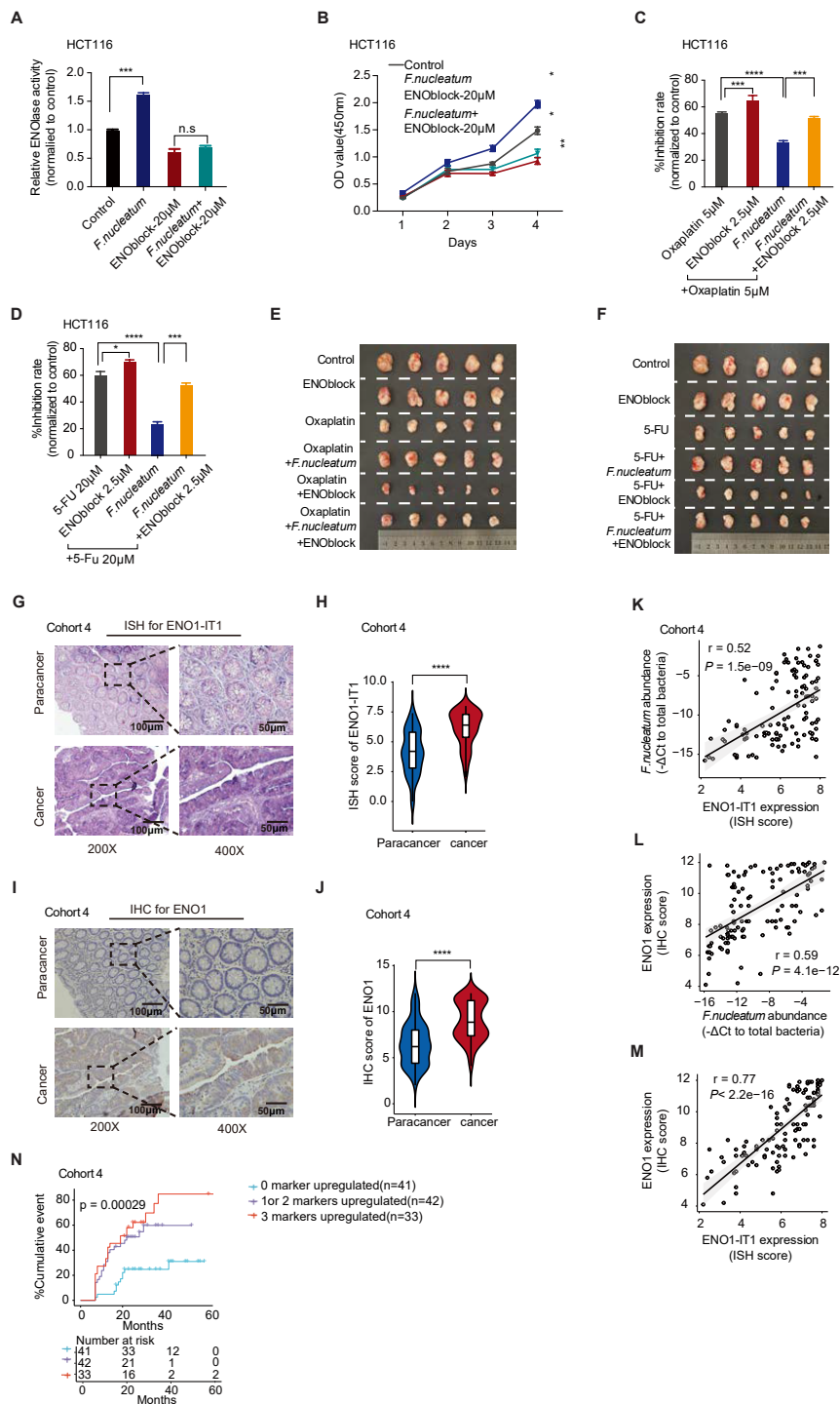


Figure 6 Levels of *F. nucleatum*, ENO1-IT1, and ENO1 correlate and predict CRC patient outcome. (A–B) ENO1ase activity normalised to control cells (A, n=6) and cell proliferation assay (B, n=6) in HCT116 cells co-cultured with *F. nucleatum* in the presence of ENOblock (20 µM), data pooled from two independent experiments. (C–D) Cell inhibition rate normalised to none-treated control cells in HCT116 cells on Oxaplatin (C, 5 µM) or 5-FU (D, 20 µM) treatment with the presence of ENOblock (2.5 µM) and *F. nucleatum*, n=6. (E–F) Representative data of tumours in mice under different conditions (E and F shared the same none-treated and ENOblock (1 mg kg⁻¹) control groups). (G) Representative images (G) and statistical analysis (H) of ENO1-IT1 expression by ISH in colorectal cancer and paired adjacent intestinal tissues in cohort 4, n=116. Bar scale=100 µm or 50 µm. (I–J) Representative images (I) and statistical analysis (J) of ENO1 expression by IHC in colorectal cancer and paired adjacent intestinal tissues in Cohort 4, n=116. Bar scale=100 µm or 50 µm. (K–M) Correlation analysis of *F. nucleatum* abundance, ENO1-IT1 and ENO1 expression in cohort 4, n=116. Pearson correlation test. (N) Kaplan-Meier analysis of disease-free survival for patients with CRC based on the number of upregulated molecular markers (ENO1, ENO1-IT1 and *F. nucleatum* abundance); n=116, Log-rank test. All data are mean±SEM *p<0.05, **p<0.01, ***p<0.001, ****p<0.0001, n.s., not significant. One-way ANOVA test in (A–D); non-parametric Mann-Whitney U test in (H, J). ANOVA, analysis of variance; CRC, colorectal cancer; ENO1-IT1, enolase 1-intronic transcript 1.

and ENO1. ENO1-IT positively correlated with ENO1 in CRC patient tumour tissues (figure 6K–M). Using ENO1, ENO1-IT1, and *F. nucleatum* as three risk factors, we tracked the cumulative recurrence rate in 116 patients with CRC (Cohort 4, online supplemental table S1). The shortest disease-free survival was detected in 33 patients with three highly expressed markers (figure 6N). Thus, the levels of *F. nucleatum*, ENO1-IT1, and ENO1 correlate in CRC and predict poor patient outcome.

DISCUSSION

High rate of glycolysis and low pH value in the tumour micro-environment is associated with increased malignant features.^{31 32} Yet, the underlying mechanistic details pertinent to the causes of such metabolic phenotype in carcinogenesis remain unclear. Understanding the mechanisms of glycolysis activation in CRC is essential to optimising current therapeutic strategies. Cancer genetic and epigenetic alterations in CRC glycolysis activation have been extensively studied.^{33 34} Disruption of the gut microbiota by antibiotic treatment leads to colonic dysbiosis and activation of colonic mucosa inflammation.³⁵ However, the potential role of gut microbiota in CRC glucose metabolism is poorly understood. Through a combination of genomic, bioinformatic, biological and in vivo model and clinical studies, we have demonstrated that glycolysis pathway is activated in patients with CRC with high amount of *F. nucleatum*, and *F. nucleatum* promotes CRC glucose metabolism and cell proliferation.

As a key pathogenic bacterium involved in the development of CRC,^{10 14–16} *F. nucleatum* could stimulate colorectal carcinogenesis. However, it is unknown whether and how *F. nucleatum* facilitated glucose metabolism in CRC. We reported that *F. nucleatum*-induced CRC cell proliferation and growth depends on glycolysis. The data consistently point to the notion that high glucose metabolism is a decisive factor for *F. nucleatum* to control human CRC aggressiveness. We have dissected the mechanisms by which *F. nucleatum* mediates glycolysis pathway activation. Epigenetic modification of DNA or RNA usually occurs during colorectal carcinogenesis via environment alteration.^{17 36 37} Our bioinformatic and functional studies have elucidated that lncRNA ENO1-IT1, which directly interacts with KAT7 and transactivates ENO1 gene, is selectively upregulated by *F. nucleatum*. *F. nucleatum* mediates glycolysis activation and cell proliferation via selectively targeting specific ENO1-IT1. Bioinformatics analysis further revealed that *F. nucleatum* might regulate glycolysis via SP1. Further function assay indicates that SP1 may directly modulate ENO1-IT1 transcription in response to *F. nucleatum* treatment. Our data is consistent with the previous report that *Fusobacterium* usually upregulates SP1 expression in human tissues.²⁶ Notably, the role of microbiota in the functional regulation of any lncRNA have not been reported in the literature. ENO1-IT1 was initially found by RNA sequencing in clear-cell renal cell carcinoma.³⁸ However, its biological function and underlying mechanism have not been reported. Here, we demonstrate that *F. nucleatum* induces transactivation of ENO1-IT1 and affects tumour glycolysis and progression.

In addition to its biological importance, our work may be relevant in clinical management of patients with CRC. We have observed that the amount of *F. nucleatum* is associated with high glucose metabolism and poor prognosis in patients with CRC. Measurement of ENO1-IT1, ENO1 and *F. nucleatum* levels may predict patient outcome. ENO1 may be a promising therapeutic target in patients with CRC with high amount of *F. nucleatum*. In the context of potential translation, ENOblock, an inhibitor of ENO1 enzyme,³⁹ effectively inhibits ENO1 activity and

glucose metabolism in CRC cells conditioned with *F. nucleatum*. Development of specific inhibitors of ENO1 may be helpful to treat patients with CRC, especially those patients with CRC with high amount of *F. nucleatum*.

In summary, we have found that *F. nucleatum* empowers tumour glucose metabolism and oncogenesis via SP1, ENO1-IT1, and KAT7 to target the key component of glycolysis pathway (eg, ENO1)(online supplemental figure S6G). Importantly, it appears that the ENO1 pathway is an actionable target via genetic and pharmacological strategies, pointing to tractable means to improve CRC therapy.

METHODS

Mice and xenograft experiments

For the xenograft experiments, BALB/c nude mice (4-week-old, male) were housed in laminar flow cabinets under specific pathogen-free conditions. To explore *F. nucleatum*-mediated metabolic reprogramming effects in CRC in vivo, we established HCT116 xenograft models. In brief, HCT116 cells (2×10^6 cells in 100 µl phosphate-buffered saline (PBS)) were injected subcutaneously into the axilla of each mouse. Seven days after subcutaneous inoculation, mice were randomly divided into indicated groups for sets of experiments.

In these experiments, the adenovirus was given by multipoint intratumoural injection two times a week for 3 weeks. Mice received intratumoural injection with *F. nucleatum*, and intraperitoneal injection with 2-DG (2.5 mM), oxaliplatin (5 mg/kg) or 5-FU (50 mg/kg) two times a week, and ENOblock (1 mg/kg, which has no effect on tumour growth in mice) every other day for 3 weeks.

To explore the role of *F. nucleatum* in glycolysis in vivo, we designed the experiments with four groups: (1) PBS (Control); (2) *F. nucleatum* bacteria solution (in PBS); (3) 2-DG; and (4) 2-DG and *F. nucleatum*.

To explore the role of *F. nucleatum* and lncRNA ENO1-IT1 in vivo, we designed four groups: (1) Control adenovirus; (2) Control adenovirus and *F. nucleatum* bacteria solution (in PBS); (3) lncRNA ENO1-IT1 adenovirus; and (4) lncRNA ENO1-IT1 adenovirus and *F. nucleatum* bacteria solution.

To explore the role of glycolysis in *F. nucleatum*-mediated chemoresistance in vivo, we designed six groups: (1) Control group; (2) ENOblock group; (3) Oxaliplatin (or 5-FU) group; (4) Oxaliplatin (or 5-FU) and *F. nucleatum* group; (5) Oxaliplatin (or 5-FU) and ENOblock group; and (6) Oxaliplatin (or 5-FU), *F. nucleatum* and ENOblock group.

The length (A) and width (B) of the tumours were measured every 3 days with callipers. Tumour volume was calculated with the formula $(A \times B^2)/2$. After 3 weeks of treatment, mice were sacrificed and subcutaneous tumours were collected, volume and weighed. The tumour volume and weight were presented as means \pm SEM ($n=8$).

Patients and clinical specimens

We studied four Cohorts of patients with CRC from Renji Hospital affiliated to Shanghai Jiaotong University School of Medicine, detailed clinical and analysis information for these Cohorts could be found in online supplemental table S1.

In brief, Cohort 1 to Cohort 3 were patients who underwent surgery between 2015 and 2019. There were 33 and 10 fresh tissues in Cohort 1 and Cohort 3, respectively. There were 130 formalin-fixed paraffin-embedded tissues (FFPE) in Cohort 2. Patients were pathologically and clinically diagnosed as primary CRC, and patients in the three Cohorts underwent

Colon

PET/CT examination before radical surgery. In addition, Cohort 4 included 116 paired FFPE tissues between 2012 and 2015. Prognosis of patients in Cohort 4 was monitored by imaging examination systems (Chest X-ray and CT), gastrointestinal endoscopy and telephone follow-up.

We performed real-time PCR for CRC-related bacteria in Cohort 1 to define which bacterium is significantly correlated with the metabolic changes in CRC tissues. We used Cohort 2 to verify whether the amount of *F. nucleatum* and *B. fragilis* are linked to metabolic changes in CRC. We performed RNA sequencing and real-time PCR in Cohort 3 to explore the potential non-coding RNAs. At last, we set ENO1-IT1, ENO1 and *F. nucleatum* amount as three risk factors for CRC recurrence in Cohort 4. And we use Cohort 4 to identify the correlation between ENO1-IT1, ENO1 and *F. nucleatum* amount, and follow-up the cumulative recurrence rate.

Bacterial strains and growth conditions

Fusobacterium nucleatum, *Enterotoxigenic Bacteroides fragilis*, *Peptostreptococcus anaerobius*, *Parvimonas micra* and *Prevotella intermedia* were purchased from American Type Culture Collection (ATCC, Manassas, Virginia; detailed identifiers in online supplemental table S2). Bacteria were cultured as previously described.¹⁰

Cell culture and treatment

Human CRC cell lines RKO, SW1116, DLD1, SW480, Caco2, LoVo, HT29 and HCT116 (ATCC; detailed identifiers in online supplemental table S2) were cultured in RPMI-1640 medium (Gibco, Carlsbad, California) supplemented with 10% fetal bovine serum (FBS) at standard condition (37°C, 5% CO₂).

For bacteria treatment, cells were seeded into 6-well plates at 2×10⁵/well 24 hours ahead and co-cultured with bacteria at specific multiplicity of infection (MOI) for 2 hours in simple medium. Then, cells were washed with PBS twice and cultured in complete medium supplied with 0.01 µg/mL metronidazole (MIC for *F. nucleatum* according to previous study)⁴⁰ to remove the bacteria, and harvested for different experiments at specific time point. In experimental control group, cells were co-cultured with non-pathogenic *E. coli* at the same MOI and time duration for further assays.

For siRNA or plasmid transfection, control or treated cells were transfected with 50 pmol siRNA (GenePharma, Shanghai, China, online supplemental table S3) or 2 µg DNA (Generay, Shanghai, China) for 6 hours, then used for different assays at specific time points.

Generation of ENO1-IT1 knockout HCT116 cell lines (HCT116 ENO1-IT1-KO)

Knockout of lnc-ENO1-IT1 in HCT116 cells was performed by the CRISPR-Cas9 genomic editing system, as previously described.^{41 42} We designed two targeting constructs with single-guide RNAs (sgRNAs) to recognise two different sites near exon2 of lnc-ENO1-IT1. The vector is pSpCas9(BB)-2A-Puro (PX459). HCT116 cells were transfected with lentiCRISPR-ENO1-IT1 and selected with puromycin. Monoclonal cell line was generated and ENO1-IT1 knockout effect was confirmed using western blot. The sequences of sgRNAs and primers are listed (table 1).

RNA extraction and real-time PCR

Total RNA was extracted with TRIzol reagent (Invitrogen, USA) according to the manual, and 1 µg of total RNA was reverse

Table 1 Sequences of sgRNAs and primers for generation of ENO1-IT1 knockout HCT116 cells

sgRNA and primers	Sequences (5'-3')
sgRNA-1 forward	CACCGAGTTCTTGGAGAGCGCCA
sgRNA-1 reverse	AAACTGGCGCTCTCAAAGAAACTC
sgRNA-2 forward	CACCGAGACCAAGTACTGGGTCTC
sgRNA-2 reverse	AAACATTTCACAGTACTGGGTCTC
ENO1-IT1 exon2 forward	TCCAGAGAAGATGTTGGAGG
ENO1-IT1 exon2 reverse	TTCTGAGTTGGAAGTCAGG
ENO1-IT1, enolase 1-intronic transcript 1; sgRNA, single-guide RNA.	

transcribed using the PrimeScript RT Reagent Kit (Perfect Real Time; Takara, Japan). Real-time PCR was performed using StepOnePlus real-time PCR system (Applied Biosystems, Foster City, California) to detect gene expression or bacterial abundance. The Ct values obtained from different samples were compared using the 2^{-ΔΔCt} method. β-actin, PGT, 18 s rRNA and 16 s rRNA were served as internal reference gene in different assays. The primers (online supplemental table S3) were provided by Sangon Company.

Detection of bacterial abundance

Genomic DNA (gDNA) was extracted from FFPE CRC tissue with QIAamp DNA FFPE Tissue Kit (QIAGEN, Hilden, Germany). gDNA from each specimen was subjected to real-time PCR to determine the abundance of interested bacteria by detecting the 16S ribosome genes (primers seen in online supplemental table S3) and analysis as previously described.¹⁰

Western blot and chemical reagents

Western blot was performed using standard techniques.⁴³ Briefly, 40 µg of protein was electrophoresed through 10% or 12% SDS polyacrylamide gels and were transferred to a PVDF membrane (Bio-Rad, USA). The membranes were incubated into primary antibodies at 4°C overnight, followed by secondary antibodies labelled with HRP (1:3000, KangChen, China) at room temperature for 1 hour. The signals were detected using ECL Kit (Pierce Biotech, Rockford, Illinois, USA). A β-actin or histone 3 antibody was used as a control for whole-cell lysates. The information on all antibodies was listed in online supplemental table S4.

Cell proliferation assay

Cell proliferation was assessed by Cell Counting kit-8 assay (Dojindo, Japan), or EdU assay (Invitrogen, USA) according to the product manual. In brief, HCT116 and DLD1 cells were seeded onto 6-well plates at 2×10⁵ cells/well and for bacteria co-culture or genetic transfection (detailed in Cell culture and treatment part). To conduct CCK8 assay, control and treated cells were seeded onto 96-well plates at 2000 cells/well and 10 µl of CCK-8 solution was added to the cells at specific time points and incubated for 2 hours at 37°C, the reaction product was quantified according to the manufacturer's instructions (OD 450 nm). For EdU assay, cells were incubated with EdU stain for 2 hours and positively-stained cells were counted via flow cytometry.

Luciferase assay

Cells were co-transfected with 1 µg of the luciferase reporter plasmids and 100 ng of the pRL-TK-Renilla-luciferase plasmid (Promega, Wisconsin, USA). Two days after transfection, cells were seeded at 10000/well and another 24 hours later, Luciferase

activities were quantified using the Dual-Luciferase Assay Kit (Promega, Wisconsin, USA), and was measured by the FLUOstar Omega software (BMG Labtech). Transfection efficiency was normalised by dividing the luciferase activity of the construct by the corresponding Renilla luciferase activity.

Adenovirus and plasmids construction

The control, control shRNA, ENO1-IT1 shRNA and ENO1 shRNA adenovirus were constructed by Shanghai Obio Technology Company (Shanghai, China). The control plasmid, ENO1-IT1 overexpressing plasmids, ENO1 overexpression plasmids were constructed by Generay Technologies (Shanghai, China).

¹⁸F-FDG PET Imaging in vivo

In vivo small animal imaging was conducted at Nuclear Medicine Department of Renji Hospital, Shanghai Jiaotong University School of Medicine. Mice were fasted for 8 hours and injected with approximately 250 µCi of ¹⁸F-FDG via lateral tail vein (the exact dose was calculated by measuring the syringe before and after injection). Mice were maintained in cages at room temperature for 1 hour and anaesthetised with isoflurane. Mice were placed on a pad in the prone position, followed by micro-PET and micro-CT imaging. ¹⁸F-FDG uptake was quantified by drawing region of interest (ROI) using IRIS PET/CT software and plotting maximum uptake values (SUVmax).

Lactate production assay and glucose uptake assay

L-Lactate Assay kit (Colorimetric) was used to measure the lactate production (Abcam 65331, Cambridgeshire, UK) and Glucose Uptake Colorimetric Assay Kit (Abcam 136955, Cambridgeshire, UK) was used to determine glucose uptake according to the manufacturer's protocols.

For lactate assay, the transfected and/or *F. nucleatum*-treated (MOI=100~200, 2~3 hour) cells (1×10^4) were planted into 96-well cell culture plates and incubated at 37°C overnight. After starvation for 2 hours, the supernatant of each group was collected and deproteinised, following by measurement of lactate production. The lactate levels were measured at 450 nm in a microplate reader. All the experiments were performed in triplicate.

For glucose uptake assays, cells were seeded into 6-well plates and transfected and/or co-cultured with *F. nucleatum* (MOI=100~200, 2~3 hour) and incubated for 24 hours. The treated cells were collected by trypsin digestion, and 1×10^4 cells were planted into 96-well cell culture plates and incubated at 37°C overnight. Then cells were starved for 2 hours and incubated with 100 µl Krebs-Ringer-Phosphate-HEPES for 40 min for the depletion of endogenous glucose, followed by 10 µl 2-DG (10 mM) incubation for 20 min. Cells were collected with extraction buffer and treated for detection of glucose uptake ability. The glucose uptake levels were measured by OD at 412 nm in a microplate reader. All the experiments were performed in bipartite.

Seahorse metabolic analysis

ECAR and OCR were measured using Seahorse XF Glycolysis Stress Test Kit and Seahorse XF Cell Mito Stress Test Kit (Agilent Technologies, Palo Alto, California). HCT116 and DLD1 cells were seeded into the XF96-well culture plates with 10^4 cells/well, and incubated at 37°C overnight for the measurement of ECAR and OCR. Measurements were conducted under the instruction of manual. Seahorse Wave software was used to analyse the data.

Mass spectrometric metabolomics analysis

For Mass Spectrometric analysis, HCT116 cells after *F. nucleatum* stimulation were collected and added with 1 mL pre-cooled methanol/acetonitrile/water (2:2:1, v/v/v). The samples were vortexed, sonicated at 4°C for 20 min and incubated at -20°C for 1 hour to precipitate proteins. The mix was centrifuged at 14 000 rcf for 10 min at 4°C and dried under vacuum. The dried samples were dissolved in 100 µL of acetonitrile-water solution (1:1, v/v) and centrifuged at 14 000 rcf for 10 min at 4°C. Electrospray ionisation was conducted using Agilent 1290 Infinity chromatography system and QTRAP 5500 (AB SCIEX) mass spectrometer.

(Fluorescent) in situ hybridisation and immunohistochemical staining

The in situ detection of ENO1-IT1 was performed on 6 µm FFPE tissue slides using DIG-labelled miRCURY Detection probe (Exiqon). The probe sequence of ENO1-IT1 is listed as follows: 5'-3' /5DigN/ AGATTCTTGAACACCAGGATA/ 3Dig_N/. Briefly, the slides were hybridised with a probe (LNA-modified and DIG-labelled oligonucleotide; Exiqon) complementary to ENO1-IT1. The hybridised probes were detected by applying nitroblue tetrazolium/5-bromo-4-chloro-3-indolyl phosphate colour substrate (Roche) to the slides. Slides were then counterstained with VECTOR nuclear fast red counterstain (Vector Laboratories). Methodologically positive control (RNU6B, Exiqon), positive controls (lncRNA GLCC1) and scrambled (negative) control RNA were included for each hybridisation procedure.

Fluorescent in situ hybridisation was performed on CRC cells using the BaseScope Reagent Kit-RED (ACD, cat.no.323110) according to the manufacturer's instructions. Briefly, 3×10^4 HCT116 and plasmid-transfected DLD1 cells were seeded into chambers, fixed by 4% PFA, dehydrated and rehydrated in ethanol. ENO1-IT1 probe, together with positive control (ACD, cat.no.701031) and negative control (ACD, cat.no.701011) probes amplification was performed according to the manufacturer's instruction, stained and mounted with DAPI for analysis, or continued to the immunohistochemical fluorescent procedure for KAT7. Immunohistochemical fluorescent was used to visualise the co-localisation of KAT7 and ENO1-IT1. Briefly, RNA-labelled cells were blocked by 5% goat serum for 1 hour before incubated with anti-KAT7 antibody (ab70183, 1:200), labelled by goat-anti-rabbit fluorescent second antibody and stained by DAPI for further investigation. The slides were visualised using a Zeiss confocal microscope.

The expression of ENO1 was examined by immunohistochemical staining with the LSAB+Kit (DakoCytomation) according to the manufacturer's instructions. The expression levels of ENO1 and ENO1-IT1 were quantified using a visual grading system based on the extent of staining (percentage of positive tumour cells) and the intensity of staining as described previously.⁴⁴

In vitro transcription and translation assay

ENO1-IT1 was cloned into pBluescript KSII downstream of the T7 promoter. The recombinant plasmids were then transcribed (Promega, USA). Then ENO1-IT1 RNA was purified in vitro and translated by Biotinylated leucine tRNA (Promega, USA). Biotinylated proteins were detected using a BrightStar BioDetect Kit (Ambion, USA). C-Myc messenger RNA (mRNA) was used as a positive translation control, water and lncRNA GLCC1 served as negative controls.

Chromatin immunoprecipitation

Chromatin immunoprecipitation was performed as follows. Chromatin was sonicated, blocked and immunoprecipitated with different primary antibodies at 4°C overnight. After immunoprecipitation, the protein-DNA cross-links were reversed and the DNA was purified. Then real-time ChIP-PCR was carried out in a 10 µL reaction volume using the eluted immunoprecipitated genomic DNA. The forward and reverse primers are listed in online supplemental table S3.

ChIP-seq was performed after knockdown of lncRNA ENO1-IT1 in HCT116 cells.

RNA immunoprecipitation

RNA immunoprecipitation (RIP) assays were conducted using the Magna RIP Kit (Millipore, New Bedford, Massachusetts) according to the manufacturer's protocols. HCT116 cells were collected using RIP lysis buffer and were immunoprecipitated using anti-KAT7 antibody and normal rabbit IgG. The co-precipitated RNAs were purified using phenol:chloroform:isoamyl alcohol, and subjected to reverse transcription-PCR or real-time PCR analysis. Meanwhile, a control amplification was carried out on the input RNA before immunoprecipitation. The gene-specific primers used for detecting lncRNA ENO1-IT1 are displayed in online supplemental table S3.

High-throughput sequencing

For RNA-seq on human tissue and cell lines, each sample was cleaned up on a RNeasy Mini Column (Qiagen, Limburg, Netherlands), treated with DNase, and analysed for quality on an Agilent 2100 Bioanalyzer. Samples were on an Illumina HiSeq 4000 platform for 2×150 bp paired-end sequencing. The sequenced reads were aligned to the human genome GRCh38 by HISAT2.⁴⁵ FeatureCounts⁴⁶ was used to quantitate the transcriptome with genome annotation GENCODE v22. Differential expression analyses were performed to the count files using DESeq2 packages, following standard normalisation procedures.⁴⁷ The RNA sequence data have been deposited in NCBI's Gene Expression Omnibus (GEO, <http://www.ncbi.nlm.nih.gov/geo/>) and are accessible through GEO Series accession number GSE139402, GSE141805.

For ChIP-Seq, chromatin was further sonicated to reduce size, and immunoprecipitated with anti-KAT7 and anti-H3K27Ac antibodies, respectively. Library generation was performed with pooled ChIP DNA samples from three independent ChIP preparations according to the Illumina protocol. Briefly, ChIP DNA fragment ends were repaired and phosphorylated using Klenow, T4 DNA polymerase and T4 polynucleotide kinase (Illumina kit components, USA). After Illumina adapters ligation, DNA was size selected by gel purification and amplified using Illumina primers. Sequencing was performed at Genenergy Inc, Shanghai, on an Illumina Hi-Seq 4000 machine. The FASTQ files were aligned to hg19 using Bowtie. Enriched regions were determined by the MACS (Model-based Analysis for ChIP-Seq) programme (<http://liulab.dfci.harvard.edu/MACS/>) with a default setting.⁴⁸ Binding and expression target analysis (BETA, V1.0.7) was used to predict peak-associated genes.⁴⁹ All sequencing tracks were viewed using the Integrated Genomic Viewer (IGV 2.3.61). All genomics data sets were deposited in GEO under accession number GSE139403.

Statistical analysis

Spearman's correlation (two-tailed) was performed using R software to determine the expression correlation between SUVmax

and enrichment of different bacterial species in figure 1A,B, or other clinical features in online supplemental figure S1D–F); to determine the expression correlation between ENO1-IT1, ENO1 and *F.nucleatum* in figure 6K–M. Statistics in figure 1C, (online supplemental figure S1C, G–L), figure 6H,J and Kaplan-Meier analysis of disease-free survival for patients with CRC in figure 6N was conducted via R software. One-way analysis of variance and Student's t-test (two tailed) of bar graphs and scatter plots in this manuscript were performed using GraphPad Prism software.

Author affiliations

¹State Key Laboratory for Oncogenes and Related Genes; Key Laboratory of Gastroenterology & Hepatology, Ministry of Health; Division of Gastroenterology and Hepatology; Shanghai Cancer Institute; Shanghai Institute of Digestive Disease, Ren Ji Hospital, School of Medicine, Shanghai Jiao Tong University, Shanghai, China

²Department of Gastrointestinal Surgery, Renji Hospital, School of Medicine, Shanghai Jiao Tong University, Shanghai, China

³Department of Nuclear Medicine, Renji Hospital, School of Medicine, Shanghai Jiao Tong University, Shanghai, China

⁴Department of Pathology, Renji Hospital, School of Medicine, Shanghai Jiao Tong University, Shanghai, China

Contributors JH, FG and SL performed most of the experiments with assistance from DM, CS, TT, XZ, YX and TS, CW, XZ and JL helped in micro PET-CT scan. TY, YC, JC, MZ and XM contributed in sample collection. YP and QL helped in pathological assays. JH, FG and SL performed most of the statistical analysis, with HC helped in analysis using R software. JH, HC, and JF conceived and supervised the study. JH, FG, and SL wrote most of the manuscript. All authors commented on the manuscript.

Funding This project was supported in part by grants from the State Key R&D Program (2020YFA0509200), National Natural Science Foundation of China (81421001, 81530072, 81830081, 81871901, 81874159, 81790632, 31970718, 81903064); the Program for Professor of Special Appointment (Eastern Scholar No. 201268) at Shanghai Institutions of Higher Learning; the Shanghai Municipal Education Commission—Gaofeng Clinical Medicine Grant (No. 20152512, 20161309); Shu Guang project supported by Shanghai Municipal Education Commission and Shanghai Education Development Foundation (17SG18); Program of Shanghai Young Academic/Technology Research Leader(19XD1422400); Shanghai Municipal Health Commission, Collaborative Innovation Cluster Project (2019CXJQ02).

Competing interests None declared.

Patient consent for publication Not required.

Ethics approval The Ethics Committees in the Renji Hospital approved the study protocols, and written informed consent was obtained prior to the investigation. All the research was carried out in accordance with the provisions of the Helsinki Declaration of 1975. All mice experiments were conducted in accordance with the National Institutes of Health Guidelines for the Care and Use of Laboratory Animals. All of the study procedures were approved by the Institutional Animal Care and Use Committee of Renji Hospital, School of Medicine, Shanghai Jiaotong University.

Provenance and peer review Not commissioned; externally peer reviewed.

Data availability statement Data are available upon reasonable request. All data relevant to the study are included in the article or uploaded as supplementary information. All data and source associated with this study are available from the corresponding author on reasonable request.

Supplemental material This content has been supplied by the author(s). It has not been vetted by BMJ Publishing Group Limited (BMJ) and may not have been peer-reviewed. Any opinions or recommendations discussed are solely those of the author(s) and are not endorsed by BMJ. BMJ disclaims all liability and responsibility arising from any reliance placed on the content. Where the content includes any translated material, BMJ does not warrant the accuracy and reliability of the translations (including but not limited to local regulations, clinical guidelines, terminology, drug names and drug dosages), and is not responsible for any error and/or omissions arising from translation and adaptation or otherwise.

ORCID iDs

Jie Hong <http://orcid.org/0000-0001-9579-0794>

Shi-Yuan Lu <http://orcid.org/0000-0002-2825-8244>

Xiong Ma <http://orcid.org/0000-0001-9616-4672>

Haoyan Chen <http://orcid.org/0000-0001-6163-8110>

Jing-Yuan Fang <http://orcid.org/0000-0003-2282-0248>

REFERENCES

- 1 Siegel RL, Miller KD, Jemal A. Cancer statistics, 2020. *CA A Cancer J Clin* 2020;70:7–30.
- 2 Siegel RL, Miller KD, Goding Sauer A, et al. Colorectal cancer statistics, 2020. *CA A Cancer J Clin* 2020;70:145–64.
- 3 Dahan L, Sadok A, Formento J-L, et al. Modulation of cellular redox state underlies antagonism between oxaliplatin and cetuximab in human colorectal cancer cell lines. *Br J Pharmacol* 2009;158:610–20.
- 4 Zou W, Wolchok JD, Chen L. Pd-L1 (B7-H1) and PD-1 pathway blockade for cancer therapy: mechanisms, response biomarkers, and combinations. *Sci Transl Med* 2016;8:328rv4.
- 5 Russo M, Crisafulli G, Sogari A, et al. Adaptive mutability of colorectal cancers in response to targeted therapies. *Science* 2019;366:1473–80. doi:10.1126/science.aav4474
- 6 Hanahan D, Weinberg RA. Hallmarks of cancer: the next generation. *Cell* 2011;144:646–74.
- 7 Warburg O. On the origin of cancer cells. *Science* 1956;123:309–14.
- 8 Rohren EM, Turkington TG, Coleman RE. Clinical applications of PET in oncology. *Radiology* 2004;231:305–32.
- 9 Kato Y, Ozawa S, Miyamoto C, et al. Acidic extracellular microenvironment and cancer. *Cancer Cell Int* 2013;13:89.
- 10 Yu T, Guo F, Yu Y, et al. *Fusobacterium nucleatum* promotes chemoresistance to colorectal cancer by modulating autophagy. *Cell* 2017;170:548–63. e16.
- 11 Kostic AD, Gevers D, Pedamallu CS, et al. Genomic analysis identifies association of *Fusobacterium* with colorectal carcinoma. *Genome Res* 2012;22:292–8.
- 12 Caglar M, Yener C, Karabulut E. Value of CT, FDG PET-CT and serum tumor markers in staging recurrent colorectal cancer. *Int J Comput Assist Radiol Surg* 2015;10:993–1002.
- 13 Wong SH, Yu J. Gut microbiota in colorectal cancer: mechanisms of action and clinical applications. *Nat Rev Gastroenterol Hepatol* 2019;16:690–704.
- 14 Abed J, Emgård JEM, Zamir G, et al. Fap2 mediates *Fusobacterium nucleatum* colorectal adenocarcinoma enrichment by binding to Tumor-Expressed Gal-GalNAc. *Cell Host Microbe* 2016;20:215–25.
- 15 Mima K, Nishihara R, Qian ZR, et al. *Fusobacterium nucleatum* in colorectal carcinoma tissue and patient prognosis. *Gut* 2016;65:1973–80.
- 16 Rubinstein MR, Wang X, Liu W, et al. *Fusobacterium nucleatum* promotes colorectal carcinogenesis by modulating E-Cadherin/β-Catenin signaling via its FadA adhesin. *Cell Host Microbe* 2013;14:195–206.
- 17 Okugawa Y, Grady WM, Goel A. Epigenetic Alterations in Colorectal Cancer: Emerging Biomarkers. *Gastroenterology* 2015;149:1204–25. e12.
- 18 Lu C, Thompson CB. Metabolic regulation of epigenetics. *Cell Metab* 2012;16:9–17.
- 19 Kinnaird A, Zhao S, Wellen KE, et al. Metabolic control of epigenetics in cancer. *Nat Rev Cancer* 2016;16:694–707.
- 20 Chen L-L. Linking long noncoding RNA localization and function. *Trends Biochem Sci* 2016;41:761–72.
- 21 Sapountzi V, Côté J. MYST-family histone acetyltransferases: beyond chromatin. *Cell Mol Life Sci* 2011;68:1147–56.
- 22 Niida H, Matsunuma R, Horiguchi R, et al. Phosphorylated HBO1 at UV irradiated sites is essential for nucleotide excision repair. *Nat Commun* 2017;8:16102.
- 23 Didiasova M, Schaefer L, Wygrecka M. When place matters: shuttling of enolase-1 across cellular compartments. *Front Cell Dev Biol* 2019;7:61.
- 24 Ke X, Fei F, Chen Y, et al. Hypoxia upregulates CD147 through a combined effect of HIF-1α and Sp1 to promote glycolysis and tumor progression in epithelial solid tumors. *Carcinogenesis* 2012;33:1598–607.
- 25 Ling Z, Liu D, Zhang G, et al. miR-361-5p modulates metabolism and autophagy via the Sp1-mediated regulation of PKM2 in prostate cancer. *Oncol Rep* 2017;38:1621–8.
- 26 Martin-Gallauxiaux C, Béguet-Crespel F, Marinelli L, et al. Butyrate produced by gut commensal bacteria activates TGF-beta1 expression through the transcription factor Sp1 in human intestinal epithelial cells. *Sci Rep* 2018;8:9742.
- 27 González OA, Li M, Ebersole JL, et al. Hiv-1 reactivation induced by the periodontal pathogens *Fusobacterium nucleatum* and *Porphyromonas gingivalis* involves Toll-like receptor 4 and 9 activation in monocytes/macrophages. *CVI* 2010;17:1417–27.
- 28 Ganapathy-Kanniappan S, Geschwind J-FH. Tumor glycolysis as a target for cancer therapy: progress and prospects. *Mol Cancer* 2013;12:152.
- 29 Icard P, Shulman S, Farhat D, et al. How the Warburg effect supports aggressiveness and drug resistance of cancer cells? *Drug Resistance Updates* 2018;38:1–11.
- 30 Wang G, Wang J-J, Yin P-H, et al. New strategies for targeting glucose metabolism-mediated acidosis for colorectal cancer therapy. *J Cell Physiol* 2019;234:348–68.
- 31 Satoh K, Yachida S, Sugimoto M, et al. Global metabolic reprogramming of colorectal cancer occurs at adenoma stage and is induced by Myc. *Proc Natl Acad Sci U S A* 2017;114:E7697–706.
- 32 Gatenby RA, Gillies RJ. Why do cancers have high aerobic glycolysis? *Nat Rev Cancer* 2004;4:891–9.
- 33 Dienstmann R, Vermeulen L, Guinney J, et al. Consensus molecular subtypes and the evolution of precision medicine in colorectal cancer. *Nat Rev Cancer* 2017;17:79–92.
- 34 Tang J, Yan T, Bao Y, et al. Lncrna GLCC1 promotes colorectal carcinogenesis and glucose metabolism by stabilizing c-myc. *Nat Commun* 2019;10:3499.
- 35 Spees AM, Wangdi T, Lopez CA, et al. Streptomycin-Induced inflammation enhances *Escherichia coli* gut colonization through nitrate respiration. *MBio* 2013;4.
- 36 Goel A, Boland CR. Epigenetics of colorectal cancer. *Gastroenterology* 2012;143:1442–60.
- 37 Lao VV, Grady WM. Epigenetics and colorectal cancer. *Nat Rev Gastroenterol Hepatol* 2011;8:686–700.
- 38 Malouf GG, Zhang J, Yuan Y, et al. Characterization of long non-coding RNA transcriptome in clear-cell renal cell carcinoma by next-generation deep sequencing. *Mol Oncol* 2015;9:32–43.
- 39 Cho H, Um J, Lee J-H, et al. ENOblock, a unique small molecule inhibitor of the non-glycolytic functions of enolase, alleviates the symptoms of type 2 diabetes. *Sci Rep* 2017;7:44186.
- 40 Bullman S, Pedamallu CS, Sicinska E, et al. Analysis of *Fusobacterium* persistence and antibiotic response in colorectal cancer. *Science* 2017;358:1443–8.
- 41 Ran FA, Hsu PD, Wright J, et al. Genome engineering using the CRISPR-Cas9 system. *Nat Protoc* 2013;8:2281–308.
- 42 Zhuo W, Liu Y, Li S, et al. Long noncoding RNA GMAN, up-regulated in gastric cancer tissues, is associated with metastasis in patients and promotes translation of ephrin A1 by competitively binding GMAN-AS. *Gastroenterology* 2019;156:676–91. e11.
- 43 Xiong H, Hong J, Du W, et al. Roles of STAT3 and ZEB1 proteins in E-cadherin down-regulation and human colorectal cancer epithelial-mesenchymal transition. *J Biol Chem* 2012;287:5819–32.
- 44 Sun T-T, He J, Liang Q, et al. Lncrna GClnC1 promotes gastric carcinogenesis and may act as a modular scaffold of WDR5 and KAT2A complexes to specify the histone modification pattern. *Cancer Discov* 2016;6:784–801.
- 45 Pertea M, Kim D, Pertea GM, et al. Transcript-Level expression analysis of RNA-Seq experiments with HISAT, StringTie and Ballgown. *Nat Protoc* 2016;11:1650–67.
- 46 Liao Y, Smyth GK, Shi W. featureCounts: an efficient General purpose program for assigning sequence reads to genomic features. *Bioinformatics* 2014;30:923–30.
- 47 Love MI, Huber W, Anders S. Moderated estimation of fold change and dispersion for RNA-Seq data with DESeq2. *Genome Biol* 2014;15:550.
- 48 Zhang Y, Liu T, Meyer CA, et al. Model-Based analysis of ChIP-Seq (MACS). *Genome Biol* 2008;9:R137.
- 49 Wang S, Sun H, Ma J, et al. Target analysis by integration of transcriptome and ChIP-Seq data with beta. *Nat Protoc* 2013;8:2502–15.